

Article

In-Situ Construction of 2D/2D ZnIn₂S₄/BiOCl Heterostructure with Enhanced Photocatalytic Activity for N₂ Fixation and Phenol Degradation

Li Guo ¹, Xuanxuan Han ¹, Kailai Zhang ¹, Yuanyuan Zhang ¹, Qiang Zhao ¹, Danjun Wang ^{1,2,*} and Feng Fu ^{1,*}

¹ College of Chemistry and Chemical Engineering, Shaanxi Key Laboratory of Chemical Reaction Engineering, Yan'an University, Yan'an 716000, China

² State Key Laboratory of Organic-Inorganic Composites Beijing Key Laboratory of Electrochemical Process and Technology for Materials, Beijing University of Chemical Technology, Beijing 100029, China

* Correspondence: wangdanjun@yau.edu.cn (D.W.); fufeng@yau.edu.cn (F.F.)

Received: 9 August 2019; Accepted: 27 August 2019; Published: 28 August 2019



Abstract: Photocatalytic nitrogen fixation and pollutants degradation at ambient temperature and pressure as a clean and efficient means represents a sustainable direction. In this paper, novel two-dimensional (2D) ZnIn₂S₄/2D BiOCl (ZIS/BOC) nanosheets heterostructures were successfully synthesized by in-situ solvothermal techniques. XPS and TEM results showed the formation of heterostructure. The photocatalytic properties of these materials were further studied by degrading phenol and nitrogen fixation under visible light irradiation. In particular, heterostructure obtained with a mass ratio of 0.5 wt % of ZnIn₂S₄ had a good application prospect and can achieve 77.4% phenol degradation rate within 6 h and a rate of ammonium production of 14.6 μmol·g_{cat}⁻¹·h⁻¹. The reaction rate of 0.5 wt % ZIS/BOC heterostructure exhibited 8.6 and 2.6 times relative to BiOCl for the degradation of phenol and nitrogen fixation, respectively. The enhanced photocatalytic activity was attributed to the collaboration of low recombination rate of photo-generated carriers and enhanced visible light absorption. Based on capture experiments and electron spin resonance (ESR) techniques, the main active species that may appear in photocatalytic systems were explored, and the corresponding photocatalytic mechanism was also proposed appropriately. This strategy will open up new ideas for the design and manufacture of more energy-efficient materials with high photocatalytic activity.

Keywords: in-situ assembly; ZnIn₂S₄/BiOCl 2D/2D heterostructure; phenol degradation; nitrogen fixation

1. Introduction

Rapid economic development and improvement of technology have an important impact on human life and quality of life. Among them, phenolic compounds have brought great convenience to human beings since they were found. However, wastewater generated in the production process is a very difficult problem and also has an indelible impact on the environment or even human health. Among phenolic-containing wastewater, phenol has the most severe toxicity. Therefore, efficient treatment of phenol compounds is of great significance to national economic and social development [1–5]. Moreover, nitrogen is widely found in nature and has an important impact on human life and quality of life. Particularly, efficient ammonia synthesis by chemical reaction involving nitrogen is of great significance to national economic and social development. The traditional Haber-Bosch process requires a lot of energy every year, so the search for a new high-efficiency, energy-saving, and environmentally-friendly nitrogen fixation method has attracted widespread public attention [6–10]. In recent decades, scientists have been working hard to find effective means to treat phenol compounds and achieve nitrogen fixation, and there has been little success [11–21].

In nature, green plants use solar light energy to assimilate carbon dioxide and water they absorb into organic matter. Photocatalytic as a kind of advanced oxidation process (AOPs) has attracted more and more attention recently because of its high efficiency and cleanness. Furthermore, photocatalytic degradation of pollutants and nitrogen fixation have been proved in various photocatalysts [22–29]. BiOCl, as one of the representatives of ternary oxides, has a special anisotropic layered structure with the band gap width is about 3.2 eV, and has good photocatalytic performance under ultraviolet irradiation, which is a bismuth-based compound with low cost, easy preparation, stable structure, and no toxicity, and has recently attracted widespread attention [30–33]. However, BiOCl itself cannot respond to visible light. Expanding its visible light response activity through effective modification methods has become the key to promote its industrial application. In order to solve these problems, a series of strategies have been developed to improve the performance of BiOCl [30–36]. Polymetallic sulfide semiconductor photocatalysis materials have been extensively studied due to their good light absorption performance and adjustable band gap [37–39]. Among many reported photocatalytic materials, ZnIn₂S₄ is a direct band gap with band energy of 2.4–2.7 eV [40,41], has shown good visible light photocatalytic performance due to its unique structure and physical and chemical properties, and has overcome the disadvantage of easy corrosion of traditional sulfides. Unfortunately, the single ZnIn₂S₄ has low transmission and separation efficiency of photogenerated carriers, and the electron (e⁻)/hole (h⁺) pair is easy to combine, thus greatly reducing its photocatalytic performance [42–44]. In view of the above factors, many researches have been carried out to try to solve the above shortcomings. Furthermore, the combination of ZnIn₂S₄ with other semiconductors to improve the photocatalytic performance of ZnIn₂S₄ has been verified [42–49].

In this work, 2D/2D ZIS/BOC heterostructures were fabricated by in-situ solvothermal methods, and under the irradiation of visible light, photocatalytic reaction was used to degrade phenol and fix nitrogen. The activity results show that the prepared ZIS/BOC heterostructures have high photocatalytic degradation of phenol and nitrogen fixation activity. The designed interface structure of ZIS/BOC heterostructures was conducive to the separation and transfer of e⁻ and h⁺, and then enhanced the photocatalytic activity. Finally, according to capture experiments and ESR techniques, the corresponding photocatalytic mechanism was proposed.

2. Results and Discussion

2.1. Characterization of Photocatalysts

The crystal structure of the prepared sample was investigated by XRD, as shown in Figure 1. The nine diffraction peaks at 2θ angles of 11.98°, 24.10°, 25.86°, 32.50°, 33.45°, 36.54°, 43.56°, 49.70°, and 58.60° correspond to (001), (002), (101), (110), (102), (003), (103), (113), and (212) crystal planes of BiOCl (JCPDS No.06-0249) [32], while the peaks at 2θ angles of 27.69°, 34.60°, 47.17°, respectively come from (102), (016), and (110) crystal planes of ZnIn₂S₄ (JCPDS No.65-2023) [44]. The 0.5 wt % ZIS/BOC heterostructure presented nearly the same XRD patterns, indicating that the coupling of ZnIn₂S₄ nanosheets showed no effect on the crystal structure of BiOCl nanosheets. However, the characteristic peaks of ZnIn₂S₄ were not observed in the composite sample, which may be due to its low relative strength or content.

Figure 2a presented the SEM image of BiOCl, where it can be seen that BiOCl is a nanosheet structure with a thickness of about 20 nm. From the inset plot of Figure 2b, it can be seen that pure ZnIn₂S₄ are nanoparticles with a size of about 10 nm. The morphology of 0.5 wt % ZIS/BOC heterostructure exhibits a novel 2D/2D heterostructure (Figure 2b), which may be due to the directional growth of ZnIn₂S₄ on the surface of 2D BiOCl structure. Figure 2c,d presented the element distribution diagram (EDS) of 0.5 wt % ZIS/BOC heterostructure. Moreover, the composite catalytic material contains six elements of Bi, Cl, O, S, In, and Zn can be seen from Figure 2e–j, the distribution of each element in the 0.5 wt % ZIS/BOC heterostructure is relatively uniform. Figure 3 exhibited the TEM electron micrographs of BiOCl and 0.5 wt % ZIS/BOC heterostructure. As can be seen from Figure 3a,b,

the BiOCl obtained has a nanosheet structure. Figure 3c,d are the TEM photographs of 0.5 wt % ZIS/BOC heterostructure. Figure 3c clearly showed a 2D/2D structure of the two compounds of BiOCl and ZnIn_2S_4 . From Figure 3d, it can be seen that the crystal plane spacing of 0.275 nm belongs to (110) crystal plane of BiOCl, and the crystal plane spacing of 0.321 nm belongs to (102) crystal plane of ZnIn_2S_4 , indicating that BiOCl and ZnIn_2S_4 form the 2D/2D heterostructure.

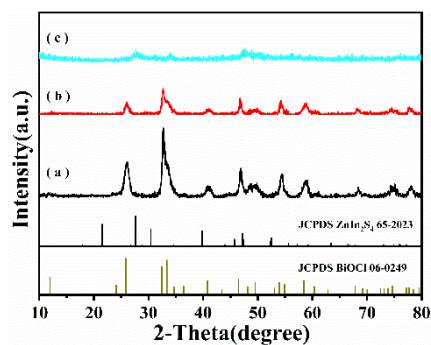


Figure 1. X-ray diffraction (XRD) patterns of (a) pure BiOCl, (b) 0.5 wt % ZIS/BOC, (c) pure ZnIn_2S_4 .

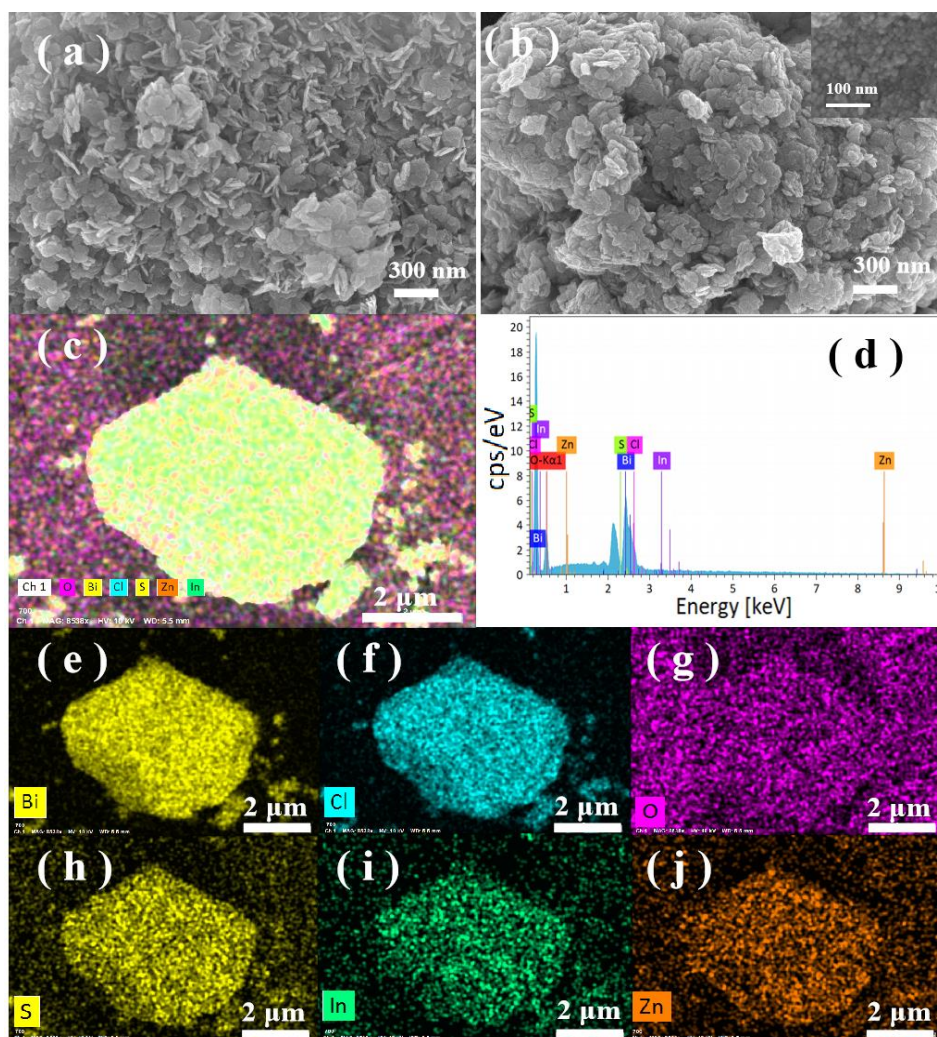


Figure 2. Scanning electron microscopy (SEM) patterns of (a) pure BiOCl, (b) 0.5 wt % ZIS/BOC and ZnIn_2S_4 (insert picture in Figure 2b), (c–j) element distribution diagram (EDS) mapping of 0.5 wt % ZIS/BOC heterostructure.

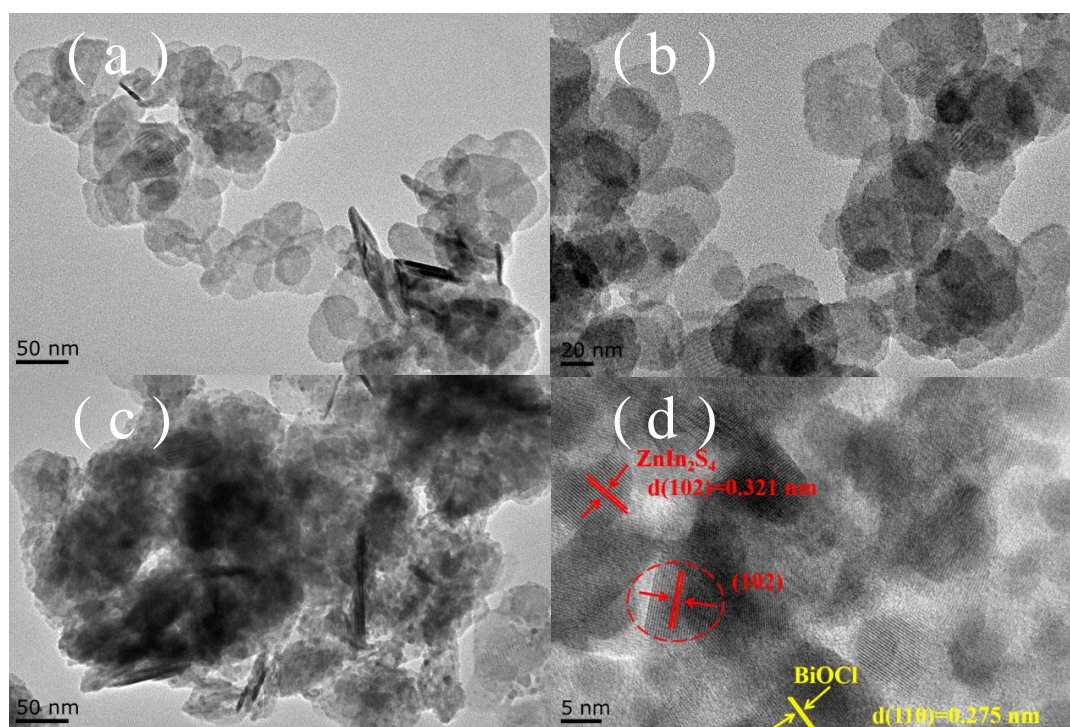


Figure 3. (a,b) Transmission electron microscopy (TEM) images of pure BiOCl and (c) 0.5 wt % ZIS/BOC heterostructure, and (d) HRTEM of 0.5 wt % ZIS/BOC heterostructure.

XPS was used to further confirm the presence of all elements in the heterostructure. Figure 4 shows the XPS spectroscopy of 0.5 wt % ZIS/BOC heterostructure, pure BiOCl, and ZnIn_2S_4 . Further analysis of Figure 4a by XPS spectroscopy revealed that the sample 0.5 wt % ZIS/BOC heterostructure contained six elements of Cl, O, Bi, Zn, In, and S. Pure BiOCl contained three elements of Cl, O, and Bi, while ZnIn_2S_4 contained three elements of Zn, In, and S. Figure 4b–g are high resolution XPS spectra corresponding to Bi 4f, O 1s, Cl 2p, Zn 2p in 3d and S 2p, respectively. Figure 4b showed that the signal peaks with binding energies of 158.8 and 164.1 eV correspond to Bi 4f_{7/2} and Bi 4f_{5/2} in the 0.5 wt % ZIS/BOC composite, indicating the presence of Bi³⁺ [50]. Figure 4c showed that the binding energy located at 530.4 and 529.5 eV are lattice oxygen and surface hydroxyl oxygen, respectively [34,51]. Figure 4d showed that the characteristic peaks with binding energies of 199.1 and 197.5 eV correspond to Cl 2p_{1/2} and Cl 2p_{3/2} [50]. It is worth noting that the peak positions of Bi 4f, O 1s, and Cl 2p in the 0.5 wt % ZIS/BOC heterostructure have a certain shift with respect to BiOCl. The shift might result from a partial e[−] transfer from ZnIn_2S_4 to BiOCl. Similarly, in Figure 4e–g, high resolution peaks of Zn 2p were not observed, and In 3d at 441.4 and 451.8 eV, respectively, indicates that it exists in the In³⁺ valence state. However, the S 2p may be because the location of binding energy is similar to that of the Bi 4f or the content is too low and not observed [43,52]. The change of banding energy of elements may be ascribed to the formation of chemical band between BiOCl and ZnIn_2S_4 . Based on the XPS results and combination of literature report [53,54], owing to the strong affinity between Bi³⁺ and S^{2−}, Bi–S bond at the interface between BiOCl and ZnIn_2S_4 may be formed during in-situ solvothermal process.

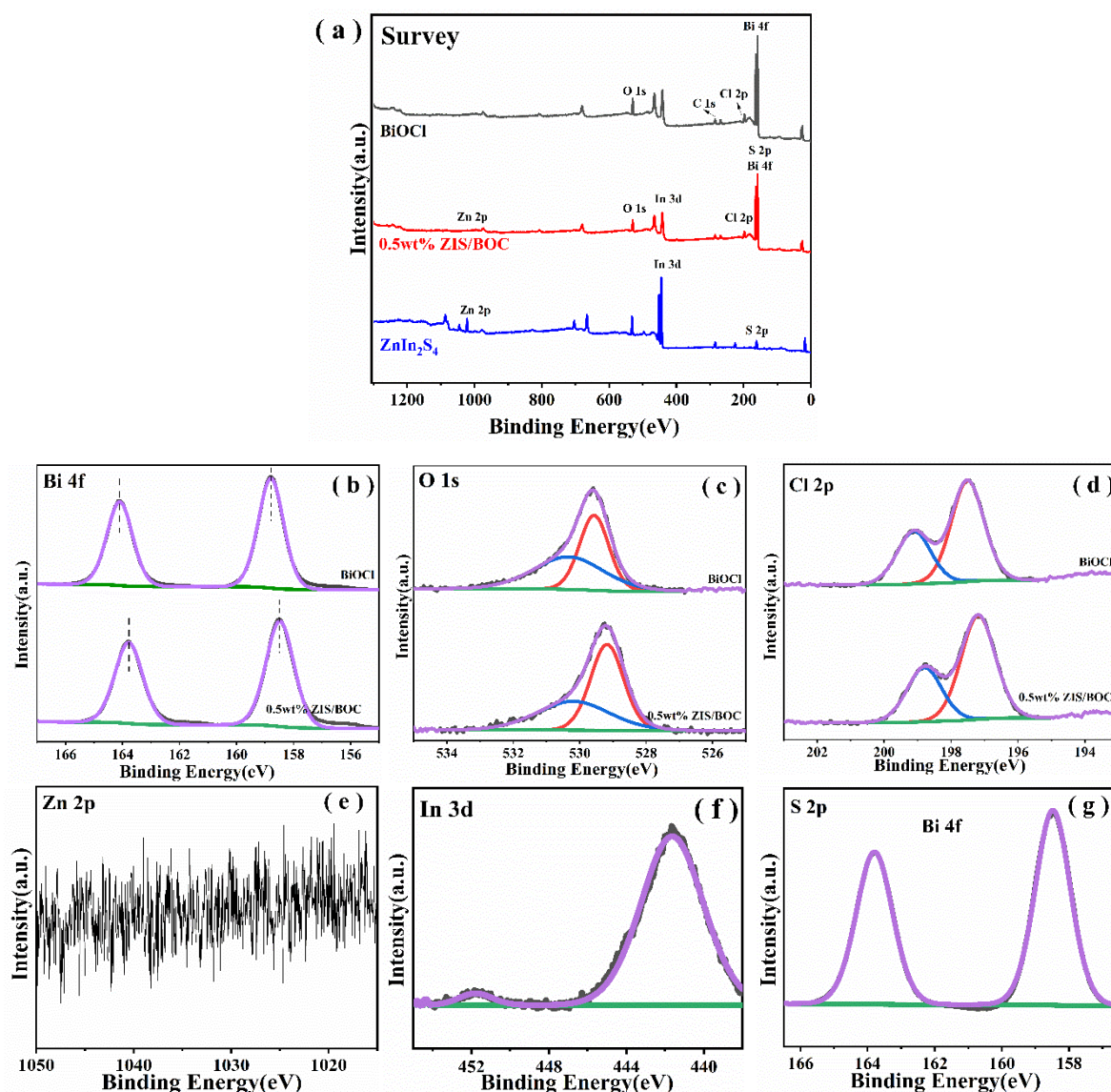


Figure 4. X-ray photoelectric spectroscopy (XPS) spectra of the BiOCl, ZnIn₂S₄ and 0.5 wt % ZIS/BOC heterostructure (a) survey, (b) Bi 4f, (c) O 1s and (d) Cl 2p of BiOCl and 0.5 wt % ZIS/BOC heterostructure, (e) Zn 2p, (f) In 3d, (g) S 2p of the 0.5 wt % ZIS/BOC heterostructure.

2.2. Optical Properties and Photocatalytic Performances of The Samples

Figure 5 are the UV-visible diffuse reflectance spectrum of the samples. As can be seen from Figure 5, BiOCl has the basic absorption edge of about 362 nm and does not respond to visible light. However, pure ZnIn₂S₄ has strong absorption in the visible light region with absorption wavelength of 566 nm. After assembling ZnIn₂S₄ nanosheets onto the surface of BiOCl nanosheets, the light response range of BiOCl was widened from 362 to 505 nm. The enhanced absorption in visible light region indicates that ZIS/BOC heterostructures can generate more photogenerated carriers compared to pure BiOCl and have potential capability for photocatalytic pollutants degradation and nitrogen fixation under visible light.

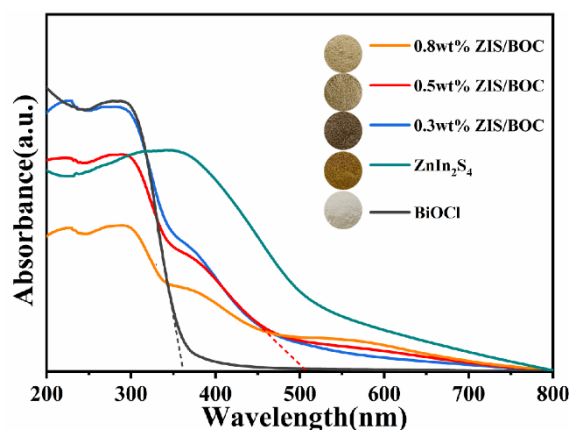


Figure 5. UV-vis diffuse reflectance spectra (UV-vis DRS spectra) of pure BiOCl, ZnIn₂S₄ and a series of ZIS/BOC heterostructures.

In order to evaluate the catalytic performance of samples, we have investigated efficacy of as-obtained BiOCl and 0.5 wt % ZIS/BOC for photocatalytic N₂ fixation. The photocatalytic experiments are performed in N₂-saturated water under the irradiation of 300 W Xe lamp in ultrapure water at ambient conditions without any sacrificial agent. Figure 6 showed the performance of photocatalytic nitrogen fixation over as-prepared catalyst under visible light irradiation. As determined by the Nessler's reagent method [55], it revealed that it can hardly produce NH₄⁺ in the presence of only catalyst or pumping N₂ alone. While the concentration of NH₄⁺ increased linearly with the extension of the illumination time (Figure 6a). Therein, 0.5 wt % ZIS/BOC heterostructure achieved a rate of ammonium production of 14.6 μmol g_{cat}⁻¹·h⁻¹, which is 2.6 folds higher than that of pure BiOCl (5.7 μmol g_{cat}⁻¹·h⁻¹). Furthermore, neither N₂H₄ nor H₂ has been detected during the photocatalytic process, implying the excellent selectivity for NH₃. It is interesting that the rate of ammonium production is low in the first half hour for BiOCl, while 0.5 wt % ZIS/BOC exhibited the same NH₄⁺ production rate during the visible light irradiation, which may be ascribed to two aspects. First, the photocatalytic N₂ fixation is a multistep reaction. The activation of N₂ may mainly occur in the first half hour by transferring the photoexcited e⁻ from BiOCl to chemisorbed N₂, dissociating N≡N bond and generating N₂H* intermediates with coupled protons [55]. Second, 0.5 wt % ZIS/BOC heterostructure may exhibit more efficient carriers transfer at the photocatalyst/solution interface than that of BiOCl, achieving faster react rate from intermediates to the final product (NH₄⁺). Also, the NH₄⁺ production rates are about 14.6, 10, 8.5 and 5.7 μmol g_{cat}⁻¹·h⁻¹, respectively, on those catalysts in an order of 0.5 wt % ZIS/BOC > 0.8 wt % ZIS/BOC > 0.3 wt % ZIS/BOC > BiOCl (Figure 6b). As can be seen from Figure 6c, the rate of ammonium production of the prepared 0.5 wt % ZIS/BOC decreased from 14.6% to 13.7% after 5 cycles, which can be attributed to deactivation of catalyst surface sites. These results clearly show that the synthesized ZIS/BOC heterostructure has higher stability.

To further investigate the photocatalytic performance of as-prepared samples, the photocatalytic degradation activity of phenol on different photocatalysts are performed as shown in Figure 7. A 300 W metal halide lamp with a wavelength of less than 420 nm cutoff was as a visible light source, and the photocatalytic activity was evaluated using phenol as a simulated pollutant. As can be seen from Figure 7a, the concentration of phenol gradually decreases with the increase of time. The analysis results showed that pure BiOCl only degraded 13.3% of phenol under visible light irradiation for 360 min, and the pure ZnIn₂S₄ degraded 31.5% of phenol, and 0.3 wt % ZIS-/BOC heterostructure, 0.5 wt % ZIS/BOC heterostructure and 0.8 wt % ZIS/BOC heterostructure degraded 55.4%, 77.4% and 57.4% of phenol, respectively, which is consistent with that of N₂ reduction. This may be due to the fact that excess ZnIn₂S₄ occupies the active site and the light-shielding effect of ZnIn₂S₄ [56]. Figure 7b is the plot of the apparent rate constants for different catalysts. It can be clearly seen that the apparent rate constant for the degradation of phenol by 0.5 wt % ZIS/BOC heterostructure is 0.00415 min⁻¹,

which is 8.6, 2.3, 1.8, and 1.7 times than that of pure BiOCl, ZnIn₂S₄, 0.3 wt % ZIS/BOC heterostructure, and 0.8 wt % ZIS/BOC heterostructure, respectively, indicating that BiOCl nanosheets modified with ZnIn₂S₄ nanosheets and can improve photocatalytic activity. Moreover, the stability was confirmed by cycle experiments using 0.5 wt % ZIS/BOC heterostructure as a photocatalyst for the degradation of phenol. As shown in Figure 8, after 5 cycles, the significant change of photocatalytic degradation rate of phenol had not been observed. In addition to this, it can be concluded that from Figure 8 that the XRD pattern after the photocatalytic reaction was approximately similar to that of the 0.5 wt % ZIS/BOC heterostructure before the photocatalytic reaction, showing that 0.5 wt % ZIS/BOC heterostructure had good stability. The activity of photocatalytic degradation of phenol by using ZnIn₂S₄/BiOCl heterostructures as photocatalyst were compared with previous literature report [57–63], as shown in Table 1. Although the as-prepared ZnIn₂S₄/BiOCl heterostructures exhibited the promoted visible-light-driven photocatalytic activities than that of pristine ZnIn₂S₄ or BiOCl, its activity still needs to be further improved by other employing strategies.

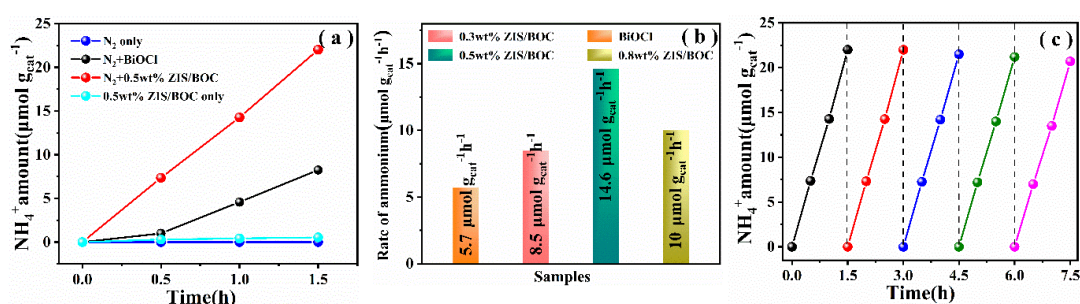


Figure 6. (a) Ammonia production amount of the BiOCl and 0.5 wt % ZIS/BOC heterostructure, (b) The rate of ammonium production on BiOCl and ZIS/BOC heterostructure. (c) Cycling times in the photocatalytic N_2 fixation over 0.5 wt % ZIS/BOC heterostructure.

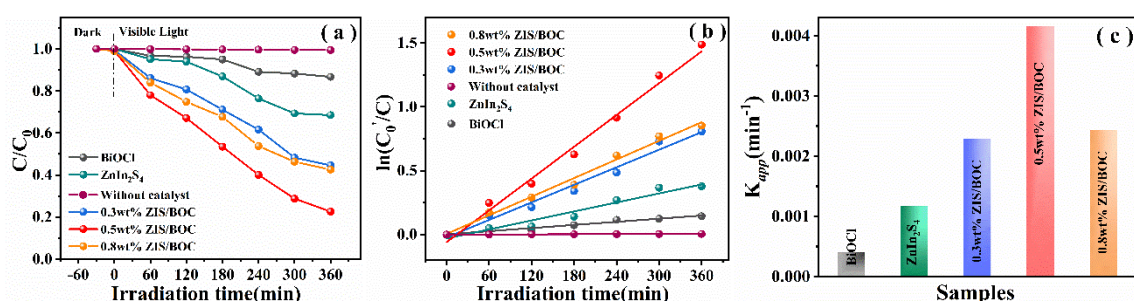


Figure 7. Photocatalytic degradation performance of BiOCl, ZnIn₂S₄ and the series of ZIS/BOC heterostructures for phenol (a), $\ln(C_0/C)$ vs. reaction time (b), the apparent rate constants (c).

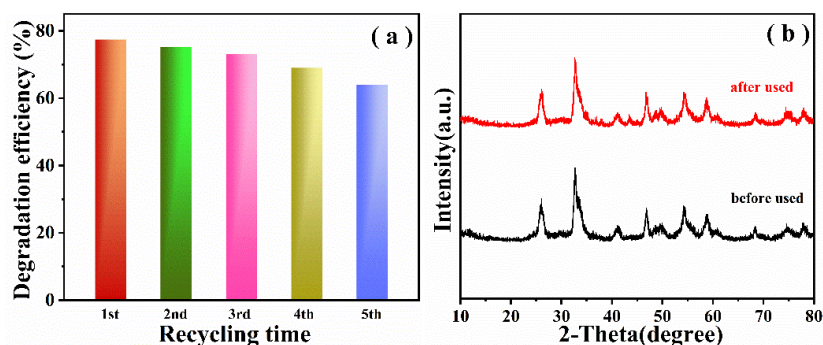


Figure 8. (a) Cycling times in the photocatalytic phenol degradation over 0.5 wt % ZIS/BOC heterostructure, (b) X-ray diffraction (XRD) pattern of 0.5 wt % ZIS/BOC heterostructure after and before used.

Table 1. Comparison of photocatalytic performance for removal of phenol.

Samples	Light Source		Organic Pollutants				Ref.
	Type ^(a)	Power (W)	Conc. ^(b) (mg·L ⁻¹)	Catalyst (g/L)	t ^(c) (time/min)	η ^(d) (%)	
ZnO	UV lamp	15	25	1.5	120	78.2	[57]
Pr-doped-TiO ₂	high-pressure mercury lamp	400	50	1.0	120	94.4	[58]
La-doped-SnO ₂	Mercury lamp	8	10	1.3	90	100	[59]
BiOCl/TiO ₂	Xe lamp	300	50	1.0	360	43	[60]
g-C ₃ N ₄ /BiOCl	Metal halide lamp	300	30	0.6	480	50	[61]
g-C ₃ N ₄ /BiOCl	LED lamp	5×24	10	1.0	150	94	[62]
ZnIn ₂ S ₄ /g-C ₃ N ₄	Xe lamp	500	10	0.4	240	72.3	[63]
0.5 wt % ZIS/BOC	Metal halide lamp	300	10	1.0	360	77.4	This work

(a) UV-lamp and mercury lamp were the UV-light sources, Xe lamp, LED lamp and metal halide lamp were the visible-light source; (b) concentration of pollutants(mg·L⁻¹); (c) irradiation time (t/min); (d) the total removal efficiency of organic pollutant (%).

2.3. Photocatalytic Mechanism

In order to further study the migration and separation efficiency of photo-generated carriers in ZIS/BOC heterostructure, fluorescence spectroscopy was performed on the prepared photocatalysts. Figure 9a showed the photoluminescence (PL) spectra of BiOCl and 0.5 wt % ZIS/BOC heterostructure at 280 nm excitation wavelength, and BiOCl has a strong fluorescence emission peak at about 391 nm. The PL intensity decreased obviously with the introduction of ZnIn₂S₄, indicating the effective separation of photoexcited e⁻ and h⁺. To reveal the generation and separation of photogenerated charges in the samples, the photoelectrochemical properties of the samples were investigated. As shown in Figure 9b, the fast photocurrent response of the sample after visible light irradiation was observed. Moreover, the photocurrent of 0.5 wt % ZIS/BOC heterostructure is higher compared with BiOCl. Figure 9c showed the impedance spectra of BiOCl and ZIS/BOC heterostructure, with an equivalent circuit model in the inset. The ohmic resistance (R₁), corresponding to the intercept with the X-axis in high frequency, includes the intrinsic resistance of the photocatalyst and the electrolyte, as well as the contact resistance at the interface between the photocatalyst and the FTO glass. The semicircle in the middle frequency range corresponds to the charge transfer resistance (R₂). The W and CPE represent the Warburg impedance and capacitance for the double layer between photocatalyst and electrolyte, respectively [64]. Comparing the Nyquist plots of BiOCl and ZIS/BOC (Figure 9c), it is found the 0.5 wt % ZIS/BOC electrode exhibits similar ohmic resistance (R₁) due to the low content of ZIS in 0.5 wt % ZIS/BOC heterostructure, while 0.5 wt % ZIS/BOC heterostructure exhibits a much lower charge transfer resistance (R₂) value (ca. 9116 Ω) than that of BiOCl (22337 Ω), implying the more efficient carriers transfer at the photocatalyst/solution interface, which is beneficial for the photocatalysis reaction [54]. Figure 10 is a schematic diagram of the effect of free radical scavenger on the photocatalytic activity of 0.5 wt % ZIS/BOC heterostructure. The three capture agents are benzoquinone (BQ, O₂⁻), ethylenediaminetetraacetic acid (EDTA, h⁺) and isopropanol (IPA, ·OH), respectively. It can be clearly seen from Figure 10 that the addition of the three capture agents had a certain effect on the degradation rate of phenol compared to the absence of the capture agent. Among them, the addition of BQ minimized the degradation of phenol, which obviously inhibited the photocatalytic degradation rate of phenol. It is concluded that O₂⁻ was the main active species for phenol degradation. For the addition of EDTA and IPA, the activity was also inhibited, confirming that h⁺ and OH were also involved in the photocatalytic reaction.

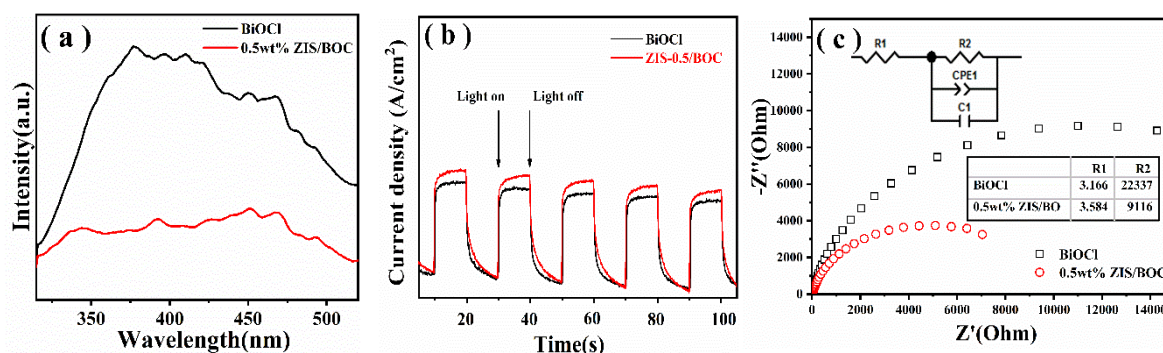


Figure 9. (a) The photoluminescence spectra, (b) Transient photocurrent response and (c) Electrochemical impedance spectroscopy (EIS) of the BiOCl and 0.5 wt % ZIS/BOC heterostructure.

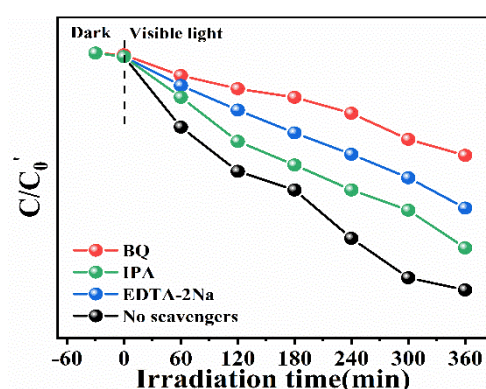


Figure 10. Photogenerated carrier trapping for degradation of phenol by 0.5 wt % ZIS/BOC heterostructure.

The ESR capture experiment further confirmed the formation of active species. As shown in Figure 11, pure BiOCl showed substantially no signal of $\cdot\text{O}_2^-$ and OH under visible light or in the dark, while 0.5 wt % ZIS/BOC heterostructure can produce significantly the typically 1:1:1 signal of O_2^- , and the four ESR signals of 1:2:2:1 signal of OH under visible light irradiation. For ZIS/BOC heterostructure, the signals of the two active species are gradually increased compared to pure BiOCl, further indicating that active species $\cdot\text{O}_2^-$ and OH were involved in the oxidative degradation of phenol. This is consistent with the captured experiments.

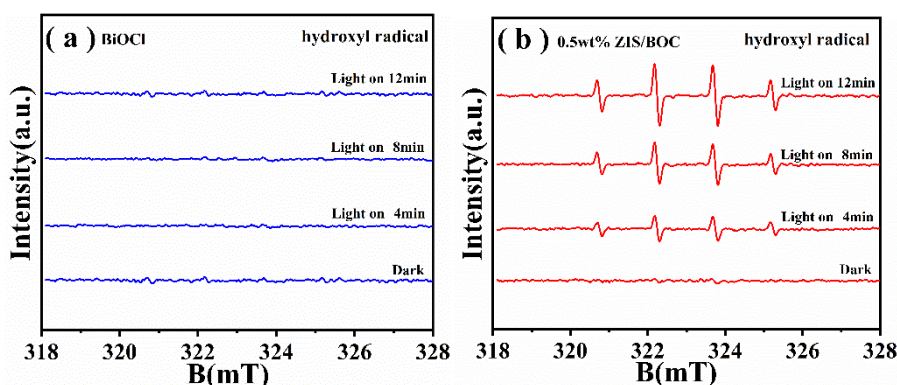


Figure 11. Cont.

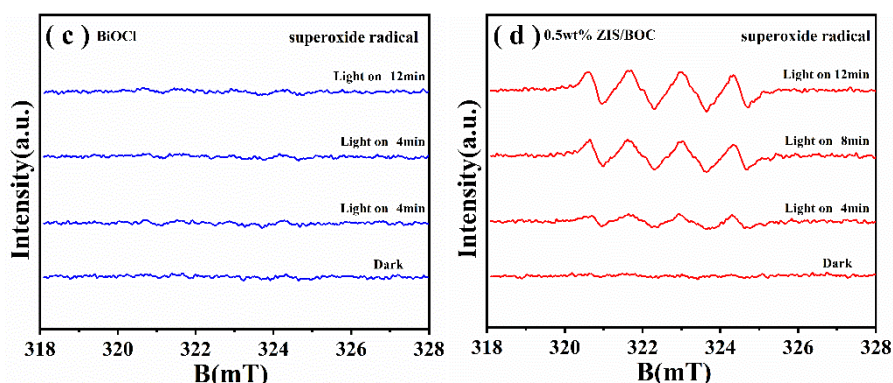


Figure 11. 5,5-dimethyl-1-pyrroline-N-oxide (DMPO) spin-trapping electrochemical impedance spectroscopy (ESR) of O_2^- and OH adducts resulting from visible light irradiation of BiOCl (a,c), and 0.5 wt % ZIS/BOC heterostructure (b,d).

The bandgap of a semiconductor can be calculated by the following formula: $(\alpha h\nu)^{1/n} = A(h\nu - E_g)$, where α , h , ν , a , and E_g respectively represent absorption coefficient, Planck constant, photon frequency, constant, and band-gap energy. Since BiOCl is an indirect transition semiconductor, it is calculated by substituting $n = 2$. Conversely, $n = 0.5$ for direct transition of ZnIn_2S_4 . The band gap of BiOCl and ZnIn_2S_4 are 3.20 and 2.61 eV, respectively (Figure 12a,b). Meanwhile, BiOCl and ZnIn_2S_4 were determined to be 1.88 and 1.25 eV, respectively, according to XPS value results (Figure 12c,d). The calculated band position of the photocatalysts were shown in Table 2.

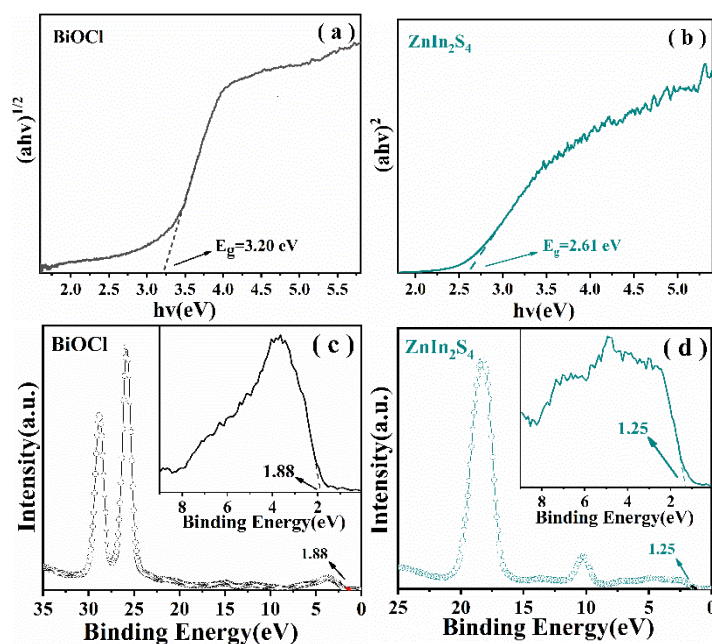


Figure 12. (a,b) the corresponding Tauc curves of the BiOCl and ZnIn_2S_4 , and (c,d) valence band spectra of the BiOCl and ZnIn_2S_4 .

Table 2. The estimated band gap energy (E_g), conduction band edge (CB), and valence band edge (VB) for BiOCl and ZnIn_2S_4 .

Semiconductor	E_g (eV)	CB (eV)	VB (eV)
BiOCl	3.20	−1.32	1.88
ZnIn_2S_4	2.61	−1.36	1.25

Figure 13 is a diagram showing the photocatalytic mechanism of the ZIS/BOC heterostructures. Appropriate conduction band and valence band positions can effectively promote the separation of photogenerated carriers when 2D BiOCl nanosheets and 2D ZnIn₂S₄ nanosheets are combined to form heterostructures. The conduction band position of ZnIn₂S₄ (−1.36 eV) is more negative than the conduction band position of BiOCl (−1.32 eV), so the conduction band e[−] of ZnIn₂S₄ can transfer to the conduction band of BiOCl. In the process of photocatalytic degradation phenol, the conduction band position of ZnIn₂S₄ (−1.36 eV) is lower than O₂/O₂[−] potential (−0.33 eV vs. NHE) so that O₂ can obtain e[−] to generate O₂[−]. However, since the valence band potential of ZnIn₂S₄ (1.25 eV) is lower than the redox potential of ·OH/OH[−] (1.99 eV) and the results of ESR and free radical trapping experiments both unexpectedly confirmed the existence of ·OH, which may be due to the partial conversion of O₂[−] to OH[−], thereby increasing the photocatalytic activity of ZIS/BOC heterostructures. The mechanism is as follows (Equations (1)–(5)):



As for the photocatalytic N₂ fixation, the conduction band position of the ZnIn₂S₄ (−1.36 eV) is more negative than E₀ (N₂/NH₃ = −0.28 eV vs. NHE), so the photogenerated e[−] can further reduce the nitrogen that adsorbed on the surface of 0.5 wt % ZIS/BOC heterostructures to NH₄⁺. In detail, the chemisorbed N₂ molecule is activated by photogenerated e[−] at the photocatalyst/solution interface [55], which is conducive to dissociating N≡N bond and generating N₂H* intermediates with coupled protons (Equation (6)), and NH₃* species are eventually generated (Equation (7)), which then exists in water. Finally, it was combined with H₂O molecules to form NH₄⁺ in succession for cycles (Equation (8)). The mechanism is as follows:

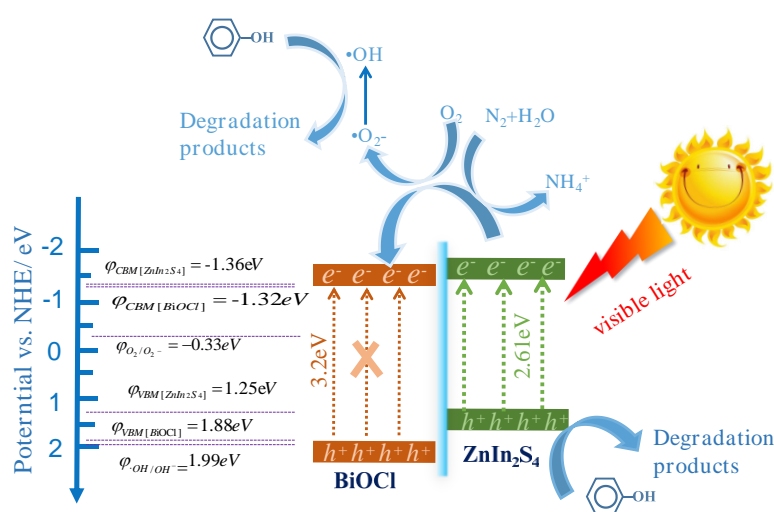


Figure 13. The photocatalytic mechanism of the phenol degradation and nitrogen fixation over photocatalyst ZIS/BOC heterostructures under visible light irradiation.

3. Experimental Section

3.1. Chemicals

All the reagents were of analytical grade and were used without any further purification.

3.2. Sample Preparation

Preparation of BiOCl nanosheets. BiOCl nanosheets were synthesized by an improved solvothermal method according to the previous report [65]. In a typical experiment, 0.9702 g (2 mmol) of $\text{Bi}(\text{NO}_3)_3 \cdot 5\text{H}_2\text{O}$ and 0.1168 g (2 mmol) of NaCl were dissolved in 10 mL of ethylene glycol respectively, and magnetically stirred for 30 min to obtain clear and transparent solutions, which are denoted as A and B respectively. Subsequently, 0.1094 g of mannitol and 0.4 g of polyvinylpyrrolidone (PVP) were dissolved in 55 mL of water to form solution C. Firstly, solution A is added drop by drop into C, and solution B is slowly added to generate white precipitate after stirring for 5 min. The mixture was then transferred to a 100 mL Teflon-lined stainless-steel autoclave for hydrothermal reaction at 160 °C for 8 h. After the reaction was finished, the autoclave was naturally cooled to room temperature, and 15% NaOH aqueous solution was added to adjust pH to 13 after washing with water. The suspension was magnetically stirred for 3 h and washed with water to neutrality. The final samples were dried at 60 °C for 8 h, and then ground to obtain BiOCl powder.

Preparation of $\text{ZnIn}_2\text{S}_4/\text{BiOCl}$ (ZIS/BOC) heterostructures. ZIS/BOC heterostructures were synthesized by an improved solvothermal method according to the previous report [66]. Firstly, 0.0036 g (0.0059 mmol) of $\text{Zn}(\text{NO}_3)_2 \cdot 6\text{H}_2\text{O}$, 0.0045 g (0.0118 mmol) of $\text{In}(\text{NO}_3)_3 \cdot 4.5\text{H}_2\text{O}$ and 0.0018 g (0.0236 mmol) of Thioacetamide (TAA) were dissolved in 30 mL of ethylene glycol solution. After 20 min of magnetic stirring, 1 g of BiOCl was added to it. After 10 min of ultrasound, magnetic stirring was continued for 30 min. Then, the mixture was transferred to a 50 mL high pressure reactor lined with polytetrafluoroethylene for solvothermal reaction at 160 °C for 3 h under programmed temperature control, and the temperature was reduced to room-temperature. The yellow powder obtained after grinding is marked as 0.5 wt % $\text{ZnIn}_2\text{S}_4/\text{BiOCl}$. The amounts of $\text{Zn}(\text{NO}_3)_2 \cdot 6\text{H}_2\text{O}$, $\text{In}(\text{NO}_3)_3 \cdot 4.5\text{H}_2\text{O}$ and TAA were changed to obtain 0.3 wt % and 0.8 wt % of composite catalyst $\text{ZnIn}_2\text{S}_4/\text{BiOCl}$ respectively. The composite catalysts were labeled as 0.3 wt % ZIS/BOC, 0.5 wt % ZIS/BOC, and 0.8 wt % ZIS/BOC. Pure ZnIn_2S_4 was prepared by the same method without the addition of BiOCl.

3.3. Characterization

X-ray diffraction (XRD) was carried out on an XRD-7000 X-ray diffractometer (Shimadzu, Kyoto, Japan), using Cu K α radiation ($\lambda = 0.15418$ nm). X-ray photoelectron spectroscopy (XPS) was recorded on a PHI-5400 X-ray photoelectron spectrometer (Physical Electronics PHI, Minnesota, America). Field emission scanning electron microscope (FESEM) images were recorded on a JSM-7610F scanning electron microscope (Japan electronics, Kyoto, Japan). Transmission electron microscopy (TEM) images were obtained on a JEM-2100 electron microscope (JEOL, Kyoto, Japan). The UV-vis diffuse reflectance spectra (UV-Vis-DRS) were measured with a UV-2550 UV-Vis spectrophotometer (Shimadzu, Kyoto, Japan). Photoluminescence (PL) spectra were measured on an F-4500 spectrophotometer (Physical Electronics PHI, Minnesota, America). Photocurrent density versus time (i-t) curves and electrochemical impedance spectroscopy (EIS) were measured on a CHI660E electrochemical workstation (Chenhua Instruments, Shanghai, China). The electron spin resonance (ESR) spectra were obtained on a JES-FA300 model spectrometer (ESR, Japan JEOL) under visible light irradiation ($\lambda \geq 420$ nm).

3.4. Photocatalytic Activity Measurement

Photocatalytic degradation experiment. In the photocatalytic degradation experiment, phenol was used as a simulated pollutant to evaluate the photocatalytic activity of the samples. A suspension containing 0.2 g of photocatalyst is added to 200 mL of 10 mg·L⁻¹ phenol solution, then placed in a photo reactor, and stirred in the dark until adsorption/desorption equilibrium is reached. A 300 W

metal halogen lamp with a 420 nm cut-off filter was chosen as the visible light source. After turning on the light source, the supernatant is taken out according to a certain time interval. Finally, the absorbance of different solution concentrations was measured by using the 4-aminonitpyrinolimetric method.

Photocatalytic Nitrogen Fixation. In nitrogen fixation experiment, a 300 W xenon lamp (with cut-off filter $\lambda < 420$ nm) was used as the light source, and a 500 mL reactor was equipped with circulating cooling water to ensure constant temperature. In general, 200 mg of photocatalyst is uniformly dispersed in 200 mL of ultrapure water, and high-purity N_2 is pumped into the reactor for 30 min to saturate the suspension and remove the dissolved oxygen under dark conditions. Subsequently, the light source was turned on, 10 mL of supernatant was taken out every 30 min, and then centrifuged at 8500 rpm for 10 min to remove the photocatalyst. The concentration of ammonia was finally measured by Nessler's reagent spectrophotometry method [55].

4. Conclusions

In conclusion, 2D BiOCl nanosheets were used as a substrate for the in-situ growth of the $ZnIn_2S_4$ nanosheets, and the carrier transport of the $ZnIn_2S_4$ is promoted based on the 2D/2D feature of the substrate. The photocatalytic phenol degradation and nitrogen fixation efficiency of ZIS/BOC heterostructures is significantly higher than that of BiOCl. It was determined that 0.5% ZIS/BOC heterostructure was the best ratio with excellent photocatalytic performance when phenol degradation was tested. The photocatalytic degradation efficiency of phenol was 77.4% and the ammonia production rate was $14.6 \mu\text{mol}\cdot\text{g}_{\text{cat}}^{-1}\cdot\text{h}^{-1}$ under visible light irradiation. The improved photocatalytic performance is attributed to the effective transfer and separation of photogenerated carriers at the interface and the enhanced light adsorb ability. The photocatalyst still maintained relatively high performance even after 5 cycles. The result of free radical trapping experiment and ESR analysis showed that O_2^- and $\cdot\text{OH}$ are the main active substances in visible light-driven catalytic system. In all, an appropriate mechanism is proposed.

Author Contributions: L.G. designed the experiments and wrote the paper; X.H. wrote the paper; K.Z., Y.Z. and Q.Z. performed the experiments and analyzed the data; D.W. and F.F. designed the experiments. All authors commented and approved the final manuscript.

Funding: This work was financially supported by the National Natural Science Foundation of China (No. 21663030, 21666039) and the Open Project of State Key Laboratory of Organic-Inorganic Composites Beijing Key Laboratory, Beijing University of Chemical Technology Beijing (No. oic-201901009) and the Project of Science & Technology Office of Shaanxi Province (No. 2018TSCXL-NY-02-01, 2013SZS20-P01) and the Project of Yan'an Science and Technology Bureau (No. 2018KG-04) and Graduate Innovation Project of Yan'an University (YCX201988).

Conflicts of Interest: The authors declare no conflict of interest.

References

1. Wang, W.; Zhou, J.; Zhang, Z.; Yu, J.; Cai, W. Different Surfactant-Assisted Hydrothermal Synthesis of Hierarchical $\gamma\text{-Al}_2\text{O}_3$ and Its Adsorption Performances for Parachlorophenol. *Chem. Eng. J.* **2013**, *233*, 168–175. [[CrossRef](#)]
2. Sun, Y.; Zhou, J.; Cai, W.; Zhao, R.; Yuan, J. Hierarchically Porous NiAl-LDH Nanoparticles as Highly Efficient Adsorbent for p-Nitrophenol from Water. *Appl. Surf. Sci.* **2015**, *349*, 897–903. [[CrossRef](#)]
3. Avetta, P.; Pensato, A.; Minella, M.; Malandrino, M.; Maurino, V.; Minero, C.; Hanna, K.; Vione, D. Activation of Persulfate by Irradiated Magnetite: Implications for the Degradation of Phenol under Heterogeneous Photo-Fenton-Like Conditions. *Environ. Sci. Technol.* **2015**, *49*, 104–1050. [[CrossRef](#)] [[PubMed](#)]
4. Fu, F.; Shen, H.D.; Sun, X.; Xue, W.W.; Shoneyec, A.; Ma, J.N.; Luo, L.; Wang, D.J.; Wang, J.G.; Tang, J.W. Synergistic Effect of Surface Oxygen Vacancies and Interfacial Charge Transfer on Fe(III)/ Bi_2MoO_6 for Efficient Photocatalysis. *Appl. Catal. B* **2019**, *247*, 150–162. [[CrossRef](#)]
5. Ding, Z.; Lu, G.Q.; Greenfield, P.F. Role of the Crystallite Phase of TiO_2 in Heterogeneous Photocatalysis for Phenol Oxidation in Water. *J. Phys. Chem. B* **2000**, *104*, 4815–4820. [[CrossRef](#)]
6. Schrauzer, G.N.; Guth, T.D. Photocatalytic Reactions. 1. Photolysis of Water and Photoreduction of Nitrogen on Titanium Dioxide. *J. Am. Chem. Soc.* **1977**, *99*, 7189–7193. [[CrossRef](#)]

7. Zhou, F.; Azofra, L.M.; Ali, M.; Kar, M.; Simonov, A.N.; McDonnell-Worth, C.; Sun, C.; Zhang, X.; MacFarlane, D.R. Electro-Synthesis of Ammonia from Nitrogen at Ambient Temperature and Pressure in Ionic Liquids. *Energy Environ. Sci.* **2017**, *10*, 2516–2520. [[CrossRef](#)]
8. Rong, X.; Mao, Y.; Xu, J.; Zhang, X.; Zhang, L.; Zhou, X.; Qiu, F.; Wu, Z. Bi₂Te₃ Sheet Contributing to the Formation of Flower-Like BiOCl Composite and Its N₂ Photofixation Ability Enhancement. *Catal. Commun.* **2018**, *116*, 16–19. [[CrossRef](#)]
9. Feng, X.; Chen, H.; Jiang, F.; Wang, X. In-Situ Self-Sacrificial Fabrication of Lanthanide Hydroxycarbonates/Graphitic Carbon Nitride heterostructures: Nitrogen Photofixation under Simulated Solar Light Irradiation. *Chem. Eng. J.* **2018**, *347*, 849–859. [[CrossRef](#)]
10. Chen, X.; Zhao, X.; Kong, Z.; Ong, W.J.; Li, N. Unravelling the Electrochemical Mechanisms for Nitrogen Fixation on Single Transition Metal Atoms Embedded in Defective Graphitic Carbon Nitride. *J. Mater. Chem. A* **2018**, *6*, 21941–21948. [[CrossRef](#)]
11. Zhang, H.; Guo, L.H.; Wang, D.; Zhao, L.; Wan, B. Light-Induced Efficient Molecular Oxygen Activation on a Cu(II)-Grafted TiO₂/Graphene Photocatalyst for Phenol Degradation. *ACS Appl. Mater. Interfaces* **2015**, *7*, 1816–1823. [[CrossRef](#)] [[PubMed](#)]
12. Pradhan, G.K.; Padhi, D.K.; Parida, K.M. Fabrication of α -Fe₂O₃ Nanorod/RGO Composite: A Novel Hybrid Photocatalyst for Phenol Degradation. *ACS Appl. Mater. Interfaces* **2013**, *5*, 9101–9110. [[CrossRef](#)] [[PubMed](#)]
13. Fu, F.; Shen, H.D.; Xue, W.W.; Zhen, Y.Z.; Soomro, R.A.; Yang, X.X.; Wang, D.J.; Xu, B.; Chi, R.A. Alkali-Assisted Synthesis of Direct Z-Scheme Based Bi₂O₃/Bi₂MoO₆ Photocatalyst for Highly Efficient Photocatalytic Degradation of Phenol and Hydrogen Evolution Reaction. *J. Catal.* **2019**, *375*, 399–409. [[CrossRef](#)]
14. Saputra, E.; Muhammad, S.; Sun, H.Q.; Ang, H.M.; Tadé, M.O.; Wang, S.B. Manganese Oxides at Different Oxidation States for Heterogeneous Activation of Peroxymonosulfate for Phenol Degradation in Aqueous Solutions. *Appl. Catal. B* **2013**, *142–143*, 729–735. [[CrossRef](#)]
15. Saputra, E.; Muhammad, S.; Sun, H.Q.; Ang, H.M.; Tadé, M.O.; Wang, S.B. Shape-Controlled Activation of Peroxymonosulfate by Single Crystal α -Mn₂O₃ for Catalytic Phenol Degradation in Aqueous Solution. *Appl. Catal. B* **2014**, *154*, 246–251. [[CrossRef](#)]
16. Luo, Y.; Chen, G.; Ding, L.; Chen, X.; Ding, L.; Wang, H. Efficient Electrocatalytic N₂ Fixation with MXene under ambient conditions. *Joule* **2019**, *3*, 1–11. [[CrossRef](#)]
17. Hoffman, B.M.; Lukoyanov, D.; Yang, Z.Y.; Dean, D.R.; Seefeldt, L.C. Mechanism of Nitrogen Fixation by Nitrogenase: The Next Stage. *Chem. Rev.* **2014**, *114*, 4041–4062. [[CrossRef](#)] [[PubMed](#)]
18. Honkala, K.; Hellman, A.; Remediakis, I.N.; Logadottir, A.; Carlsson, A.; Dahl, S.; Christensen, C.H.; Nørskov, J.K. Ammonia Synthesis from First-Principles Calculations. *Science* **2005**, *307*, 555–558. [[CrossRef](#)] [[PubMed](#)]
19. Tanabe, Y.; Nishibayashi, Y. Developing More Sustainable Processes for Ammonia Synthesis. *Coord. Chem. Rev.* **2013**, *257*, 2551–2564. [[CrossRef](#)]
20. Sivasankar, C.; Baskaran, S.; Tamizmani, M.; Ramakrishna, K. Lessons Learned and Lessons to be Learned for Developing Homogeneous Transition Metal Complexes Catalyzed Reduction of N₂ to Ammonia. *J. Organomet. Chem.* **2014**, *752*, 44–58. [[CrossRef](#)]
21. Ma, H.; Shi, Z.; Li, Q.; Li, S. Preparation of Graphitic Carbon Nitride with Large Specific Surface Area and Outstanding N₂ Photofixation Ability via a Dissolve-Regrowth Process. *J. Phys. Chem. Solids* **2016**, *99*, 51–58. [[CrossRef](#)]
22. Qiu, P.; Xu, C.; Zhou, N.; Chen, H.; Jiang, F. Metal-Free Black Phosphorus Nanosheets-Decorated Graphitic Carbon Nitride Nanosheets with C-P Bonds for Excellent Photocatalytic Nitrogen Fixation. *Appl. Catal. B* **2018**, *221*, 27–35. [[CrossRef](#)]
23. Liu, Y.; Kong, J.; Yuan, J.; Zhao, W.; Zhu, X.; Sun, C.; Xie, J. Enhanced Photocatalytic Activity over Flower-like Sphere Ag/Ag₂CO₃/BiVO₄ Plasmonic Heterostructure Photocatalyst for Tetracycline Degradation. *Chem. Eng. J.* **2018**, *331*, 242–254. [[CrossRef](#)]
24. Jiang, B.; Wang, Y.; Wang, J.; Tian, C.; Li, W.; Feng, Q.; Pan, Q.; Fu, H. In Situ Fabrication of Ag/Ag₃PO₄/Graphene Triple Heterostructure Visible-Light Photocatalyst Through Graphene-assisted Reduction Strategy. *ChemCatChem* **2013**, *5*, 1359–1367. [[CrossRef](#)]
25. Ma, D.K.; Guan, M.L.; Liu, S.S.; Zhang, Y.Q.; Zhang, C.W.; He, Y.X.; Huang, S.M. Controlled Synthesis of Olive-shaped Bi₂S₃/BiVO₄ Microspheres through a Limited Chemical Conversion Route and Enhanced Visible-Light-Responding Photocatalytic Activity. *Dalton Trans.* **2012**, *41*, 5581–5586. [[CrossRef](#)] [[PubMed](#)]

26. Guo, Y.; Li, J.; Gao, Z.; Zhu, X.; Liu, Y.; Wei, Z.; Zhao, W.; Sun, C. A Simple and Effective Method for Fabricating Novel p–n Heterostructure Photocatalyst g-C₃N₄/Bi₄Ti₃O₁₂ and Its Photocatalytic Performances. *Appl. Catal. B* **2016**, *192*, 57–71. [[CrossRef](#)]
27. Miyama, H.; Fujii, N.; Nagae, Y. Heterogeneous Photocatalytic Synthesis of Ammonia from Water and Nitrogen. *Chem. Phys. Lett.* **1980**, *74*, 523–524. [[CrossRef](#)]
28. Endoh, E.; Leland, J.K.; Bard, A.J. Heterogeneous Photoreduction of Nitrogen to Ammonia on Tungsten Oxide. *J. Phys. Chem.* **1986**, *90*, 6223–6226. [[CrossRef](#)]
29. Hu, S.Z.; Chen, X.; Li, Q.; Li, F.Y.; Fan, Z.P.; Wang, H.; Wang, Y.J.; Zheng, B.H.; Wu, G. Fe³⁺ Doping Promoted N₂ Photofixation Ability of Honeycombed Graphitic Carbon Nitride: The Experimental and Density Functional Theory Simulation Analysis. *Appl. Catal. B* **2017**, *201*, 58–69. [[CrossRef](#)]
30. Jiang, J.; Zhao, K.; Xiao, X.Y.; Zhang, L.Z. Synthesis and Facet-Dependent Photoreactivity of BiOCl Single Crystalline Nanosheets. *J. Am. Chem. Soc.* **2012**, *134*, 4473–4476. [[CrossRef](#)]
31. Jiang, R.R.; Wu, D.H.; Lu, G.H.; Yan, Z.H.; Liu, J.C.; Zhou, R.R.; Matthew, N. Fabrication of Fe₃O₄ Quantum Dots Modified BiOCl/BiVO₄ p–n Heterostructure to Enhance Photocatalytic Activity for Removing Broad-Spectrum Antibiotics under Visible Light. *J. Taiwan Inst. Chem. Eng.* **2019**, *96*, 681–690. [[CrossRef](#)]
32. Guan, M.L.; Xiao, C.; Zhang, J.; Fan, S.J.; An, R.; Cheng, Q.M.; Xie, J.F.; Zhou, M.; Ye, B.J.; Xie, Y. Vacancy Associates Promoting Solar-Driven Photocatalytic Activity of Ultrathin Bismuth Oxychloride Nanosheets. *J. Am. Chem. Soc.* **2013**, *135*, 10411–10417. [[CrossRef](#)] [[PubMed](#)]
33. Deng, F.; Zhang, Q.; Yang, L.X.; Luo, X.B.; Wang, A.J.; Luo, S.L.; Dionysiou, D.D. Visible Light-Responsive Graphene-Functionalized Bi-Bridge Z-Scheme Black BiOCl/Bi₂O₃ Heterostructure with Oxygen Vacancy and Multiple Charge Transfer Channels for Efficient Photocatalytic Degradation of 2-Nitrophenol and Industrial Wastewater Treatment. *Appl. Catal. B* **2018**, *238*, 61–69. [[CrossRef](#)]
34. Wu, X.; Zhang, K.; Zhang, G.; Yin, S. Facile Preparation of BiOX (X = Cl, Br, I) Nanoparticles and up-Conversion Phosphors/BiOBr Composites for Efficient Degradation of NO Gas: Oxygen Vacancy Effect and Near Infrared Light Responsive Mechanism. *Chem. Eng. J.* **2017**, *325*, 59–70. [[CrossRef](#)]
35. Ye, L.; Liu, J.; Gong, C.; Tian, L.; Peng, T.; Zan, L. Two Different Roles of Metallic Ag on Ag/AgX/BiOX (X = Cl, Br) Visible Light Photocatalysts: Surface Plasmon Resonance and Z-Scheme Bridge. *ACS Catal.* **2012**, *2*, 1677–1683. [[CrossRef](#)]
36. Myung, Y.; Wu, F.; Banerjee, S.; Park, J.; Banerjee, P. Electrical Conductivity of p-Type BiOCl Nanosheets. *Chem. Commun.* **2015**, *51*, 2629–2632. [[CrossRef](#)]
37. Yao, L.; Wei, D.; Ni, Y.; Yan, D.; Hu, C. Surface Localization of CdZnS Quantum Dots onto 2D g-C₃N₄ Ultrathin Microribbons: Highly Efficient Visible Light-Induced H₂-Generation. *Nano Energy* **2016**, *26*, 248–256. [[CrossRef](#)]
38. Jing, L.; Xu, Y.; Xie, M.; Liu, J.; Deng, J.; Huang, L.; Xu, H.; Li, H. Three Dimensional Polyaniline/MgIn₂S₄ Nanoflower Photocatalysts Accelerated Interfacial Charge Transfer for the Photoreduction of Cr(VI), Photodegradation of Organic Pollution and Photocatalytic H₂ Production. *Chem. Eng. J.* **2019**, *360*, 1601–1612. [[CrossRef](#)]
39. Gou, X.L.; Cheng, F.Y.; Shi, Y.H.; Zhang, L.; Peng, S.J.; Chen, J.; Shen, P.W. Shape-Controlled Synthesis of Ternary Chalcogenide ZnIn₂S₄ and CuIn(S,Se)₂ Nano-/Microstructures via Facile Solution Route. *J. Am. Chem. Soc.* **2006**, *128*, 7222–7229. [[CrossRef](#)]
40. Zhou, M.; Liu, Z.H.; Song, Q.G.; Li, X.F.; Chen, B.W.; Liu, Z.F. Hybrid 0D/2D Edamame Shaped ZnIn₂S₄ Photoanode Modified by Co-Pi and Pt for Charge Management towards Efficient Photoelectrochemical Water Splitting. *Appl. Catal. B* **2019**, *244*, 188–196. [[CrossRef](#)]
41. Fan, B.; Chen, Z.; Liu, Q.; Zhang, Z.; Fang, X. One-Pot Hydrothermal Synthesis of Ni-Doped ZnIn₂S₄ Nanostructured Film Photoelectrodes with Enhanced Photoelectrochemical Performance. *Appl. Surf. Sci.* **2016**, *370*, 252–259. [[CrossRef](#)]
42. Guan, Z.; Pan, J.; Li, Q.; Li, G.; Yang, J. Boosting Visible-Light Photocatalytic Hydrogen Evolution with an Efficient CuInS₂/ZnIn₂S₄ 2D/2D Heterostructure. *ACS Sustain. Chem. Eng.* **2019**, *7*, 7736–7742. [[CrossRef](#)]
43. Kale, S.B.; Kalubarme, R.S.; Mahadadalkar, M.A.; Jadhav, H.S.; Bhirud, A.P.; Ambekar, J.D.; Park, C.J.; Kale, B.B. Hierarchical 3D ZnIn₂S₄/Graphene Nano-Heterostructures: Their in Situ Fabrication with Dual Functionality in Solar Hydrogen Production and As Anodes for Lithium Ion Batteries. *Phys. Chem. Chem. Phys.* **2015**, *17*, 31850–31861. [[CrossRef](#)] [[PubMed](#)]

44. Yang, C.; Li, Q.; Xia, Y.; Lv, K.; Li, M. Enhanced Visible-Light Photocatalytic CO₂ Reduction Performance of ZnIn₂S₄ Microspheres by Using CeO₂ as Cocatalyst. *Appl. Surf. Sci.* **2019**, *464*, 388–395. [[CrossRef](#)]
45. Yang, G.; Chen, D.M.; Ding, H.; Feng, J.J.; Zhang, J.Z.; Zhu, Y.F.; Hamid, S.; Bahnemann, D.W. Well-Designed 3D ZnIn₂S₄ Nanosheets/TiO₂ Nanobelts as Direct Z-Scheme photocatalysts for CO₂ Photoreduction into Renewable Hydrocarbon Fuel with High Efficiency. *Appl. Catal. B* **2017**, *219*, 611–618. [[CrossRef](#)]
46. Chai, B.; Peng, T.Y.; Zeng, P.; Zhang, X.H. Preparation of a MWCNTs/ZnIn₂S₄ Composite and Its Enhanced Photocatalytic Hydrogen Production under Visible-Light Irradiation. *Dalton Trans.* **2012**, *41*, 1179–1186. [[CrossRef](#)] [[PubMed](#)]
47. Zhang, Z.Z.; Huang, L.; Zhang, J.J.; Wang, F.J.; Xie, Y.Y.; Shang, X.T.; Go, Y.Y.; Zhao, H.B.; Wang, X.X. In Situ Constructing Interfacial Contact MoS₂/ZnIn₂S₄ Heterostructure for Enhancing Solar Photocatalytic Hydrogen Evolution. *Appl. Catal. B* **2018**, *233*, 112–119. [[CrossRef](#)]
48. Yuan, Y.J.; Chen, D.Q.; Zhong, J.S.; Yang, L.X.; Wang, J.J.; Liu, M.J.; Tu, W.G.; Yu, Z.T.; Zou, Z.G. Interface Engineering of a Noble-metal-free 2D–2D MoS₂/Cu-ZnIn₂S₄ Photocatalyst for Enhanced Photocatalytic H₂ Production. *J. Mater. Chem. A* **2017**, *5*, 15771. [[CrossRef](#)]
49. Sun, W.X.; Wei, N.; Cui, H.Z.; Lin, Y.; Wang, X.Z.; Tian, J.; Li, J.; Wen, J. 3D ZnIn₂S₄ Nanosheet/TiO₂ Nanowire Arrays and Their Efficient Photocathodic Protection for 304 Stainless Steel. *Appl. Surf. Sci.* **2018**, *434*, 1030–1039. [[CrossRef](#)]
50. Gao, X.Y.; Tang, G.B.; Peng, W.; Guo, Q.; Luo, Y.M. Surprise in the Phosphate Modification of BiOCl with Oxygen Vacancy: In Situ Construction of Hierarchical Z-Scheme BiOCl-OV-BiPO₄ Photocatalyst for the Degradation of Carbamazepine. *Chem. Eng. J.* **2019**, *360*, 1320–1329. [[CrossRef](#)]
51. Wang, D.J.; Guo, L.; Zhen, Y.Z.; Yue, L.L.; Xue, G.L.; Fu, F. AgBr Quantum Dots Decorated Mesoporous Bi₂WO₆ Architectures with Enhanced Photocatalytic Activities for Methylene Blue. *J. Mater. Chem. A* **2014**, *2*, 11716–11727. [[CrossRef](#)]
52. Ruan, X.W.; Hu, H.; Che, H.N.; Jiang, E.H.; Zhang, X.X.; Liu, C.B.; Che, G.B. A Visible-Light-Driven Z-scheme CdS/Bi₁₂GeO₂₀ Heterostructure with Enhanced Photocatalytic Degradation of Various Organics and the Reduction of Aqueous Cr(VI). *J. Colloid Interface Sci.* **2019**, *543*, 317–327. [[CrossRef](#)] [[PubMed](#)]
53. Bhoi, Y.P.; Mishra, B.G. Single Step Combustion Synthesis, Characterization and Photocatalytic Application of α-Fe₂O₃-Bi₂S₃ Heterojunction for Efficient and Selective Reduction of Structurally Diverse Nitroarenes. *Chem. Eng. J.* **2017**, *316*, 70–81. [[CrossRef](#)]
54. Luo, S.; Ke, J.; Yuan, M.Q.; Zhang, Q.; Xie, P.; Deng, L.D.; Wang, S.B. CuInS₂ Quantum Dots Embedded in Bi₂WO₆ Nanoflowers for Enhanced Visible Light Photocatalytic Removal of Contaminants. *Appl. Catal. B* **2017**, *221*, 215–222. [[CrossRef](#)]
55. Zhang, N.; Jalil, A.; Wu, D.X.; Chen, S.M.; Liu, Y.F.; Gao, C.; Ye, W.; Qi, Z.M.; Ju, H.X.; Wang, C.M.; et al. Refining Defect States in W₁₈O₄₉ by Mo Doping: A Strategy for Tuning N₂ Activation towards Solar-Driven Nitrogen Fixation. *J. Am. Chem. Soc.* **2018**, *140*, 9434–9443. [[CrossRef](#)] [[PubMed](#)]
56. Ran, J.R.; Guo, W.W.; Wang, H.L.; Zhu, B.C.; Yu, J.G.; Qiao, S.Z. Metal-Free 2D/2D Phosphorene/g-C₃N₄ Van der Waals Heterojunction for Highly Enhanced Visible-Light Photocatalytic H₂ Production. *Adv. Mater.* **2018**, *30*, 1800128. [[CrossRef](#)] [[PubMed](#)]
57. Dewidar, H.; Nosier, S.A.; El-Shazly, A.H. Photocatalytic Degradation of Phenol Solution using Zinc Oxide/UV. *J. Chem. Health Saf.* **2018**, *25*, 2–11. [[CrossRef](#)]
58. Chiou, C.H.; Juang, R.S. Photocatalytic Degradation of Phenol in Aqueous Solutions by Pr-Doped TiO₂ Nanoparticles. *J. Hazard. Mater.* **2007**, *149*, 1–7. [[CrossRef](#)]
59. Al-Hamdi, A.M.; Sillanpää, M.; Dutta, J. Photocatalytic Degradation of Phenol in Aqueous Solution by Rare Earth-Doped SnO₂ Nanoparticles. *J. Mater. Sci.* **2014**, *49*, 5151–5159. [[CrossRef](#)]
60. Sánchez-Rodríguez, D.; Medrano, M.G.M.; Remita, H.; Escobar-Barríos, V. Photocatalytic Properties of BiOCl-TiO₂ Composites for Phenol Photodegradation. *J. Environ. Chem. Eng.* **2018**, *6*, 1601–1612. [[CrossRef](#)]
61. Li, Q.B.; Zhao, X.; Yang, J.; Jia, C.J.; Jin, Z.; Fan, W.L. Exploring the Effects of Nanocrystal Facet Orientations in g-C₃N₄/BiOCl Heterostructures on Photocatalytic Performance. *Nanoscale* **2015**, *7*, 18971–18983. [[CrossRef](#)] [[PubMed](#)]
62. Cai, L. Enhanced Visible Light Photocatalytic Activity of BiOCl by Compositing with g-C₃N₄. *Mater. Res. Innov.* **2015**, *19*, 392–396. [[CrossRef](#)]

63. Liu, H.; Jin, Z.T.; Xu, Z.Z.; Zhang, Z.; Ao, D. Fabrication of ZnIn₂S₄-G-C₃N₄ Sheet-On-Sheet Nanocomposites for Efficient Visible-Light Photocatalytic H₂ Evolution and Degradation of Organic Pollutants. *RSC Adv.* **2015**, *5*, 97951–97961. [[CrossRef](#)]
64. Liu, H.; Jia, M.Q.; Sun, N.; Cao, B.; Chen, R.J.; Zhu, Q.Z.; Wu, F.; Qiao, N.; Xu, B. Nitrogen-Rich Mesoporous Carbon as Anode Material for High Performance Sodium-Ion Batteries. *ACS Appl. Mater. Interfaces* **2015**, *7*, 27124–27130. [[CrossRef](#)] [[PubMed](#)]
65. Li, B.X.; Shao, L.Z.; Wang, R.S.; Dong, X.P.; Zhao, F.G.; Gao, P.; Li, Z.Q. Interfacial Synergism of Pd-Decorated BiOCl Ultrathin Nanosheets for the Selective Oxidation of Aromatic Alcohols. *J. Mater. Chem. A* **2018**, *6*, 6344–6355. [[CrossRef](#)]
66. Lin, B.; Li, H.; An, H.; Hao, W.B.; Wei, J.J.; Dai, Y.Z.; Ma, C.S.; Yang, G.D. Preparation of 2D/2D g-C₃N₄ Nanosheet@ZnIn₂S₄ Nanoleaf Heterostructures with Well-Designed High-Speed Charge Transfer Nanochannels towards High-Efficiency Photocatalytic Hydrogen Evolution. *Appl. Catal. B* **2018**, *220*, 542–552. [[CrossRef](#)]



© 2019 by the authors. Licensee MDPI, Basel, Switzerland. This article is an open access article distributed under the terms and conditions of the Creative Commons Attribution (CC BY) license (<http://creativecommons.org/licenses/by/4.0/>).